Paris Lodron Universität Salzburg

Seminar Paper

TIME-SERIES ANALYSIS OF SNOW COVER AREA (SCA) AND LAND SURFACE TEMPERATURE (LST) IN AUSTRIA SKIING AREAS WITH GOOGLE EARTH ENGINE (GEE)

Analysis and Modelling (Remote Sensing)

Supervised by

Hannah Lucille Augustin, Zahra Dabiri, Stefan Lang, Dirk Tiede

Written by

Felipe Camacho Hurtado

Registration Number: 12214476

Salzburg, July 2023

CONTENT

FIGURES & TABLES

ABBREVIATIONS

AOI	Area of Interest
AOI-1	Skiwelt Wilder Kaiser – Brixental
AOI-2	Komperdell
ESA	European Space Agency
GDP	Gross Domestic Product
GEE	Google Earth Engine
LST	Land Surface Temperature
NDSI	Normalized Difference Snow Index
OLI	Operational Land Imager
SCA	Snow-Covered Area
SWIR	Short-Wave Infrared
TIR	Thermal Infrared
TIRS	Thermal Infrared Sensor

ABSTRACT

The reduction of Snow-Covered Area (SCA) is one of the biggest challenges for the skiing industry, tourism, and ecology of Alpine regions. Addressing this issue with short-term solutions like artificial snow, water injection, and thermal blankets is not enough. As a result, it is necessary to understand the status of SCA and the impact of Land Surface Temperature (LST) increases on snow melting and generation rates, to achieve long-term solutions. The objective of this article is to explore the advantages and usability of remote sensing data and techniques, within the Google Earth Engine (GEE) cloud-computing platform, to identify SCA and LST trends and relationships through time-series analyses, allowing a deep understanding of SCA challenges and LST effects. The study focuses on the "Skiwelt Wilder Kaiser – Brixental" and "Komperdell" Austrian skiing areas between August 1, 2018, and July 30, 2023. The workflow involves calculating the Normalized Difference Snow Index (NDSI) from Sentinel 2 imagery for SCA values and generating time-series charts. Additionally, Landsat 8 Thermal Infrared (TIR) band 10 is used to measure LST. Results show LST and SCA tendencies, with high-altitude skiing resorts exhibiting more resistance to LST changes and higher SCA associated with LST decreases. Due to limitations in the analysis and validation, the study is not conclusive, but it lays the foundation for further research in this topic.

KEY WORDS: Cloud-Computing, Google Earth Engine (GEE), Austrian alps, Ski resorts, Snow, Normalized Difference Snow Index (NDSI), Land Surface Temperature (LST), Time-Series.

1. INTRODUCTION

Skiing is one of the most essential industries in the European Alps. Specifically, In the Austrian scenario, by 2020, it represented 3% of its Gross Domestic Product (GDP) (Hruby, 2020) and generated more than EUR 5.9 billion by 2018 (Wiertschaftskammer Osterreich [WOK], 2021). In fact, Austria is the European country with the largest supply of hotel accommodations in skiing areas, with more than 254 resorts that receive an average of 51.7 million skiers per year (Moreno-Gené et al, 2018). The ski tourism industry also contributes to economic activities like transportation, restaurants, and sports equipment sales (Moreno-Gené et al, 2018). Considering the mentioned economic importance of the skiing industry, governments and citizens are highly interested in the continuous demand for winter tourism, which is dependent on factors such as prices, transportation, cost, and climate change (Falk, 2010).

The public and researchers are particularly concerned about the effect of climate change, and whether winter tourism would still be economically sustainable in a world with increasing temperatures (Breiling & Charamza, 1999). This is a major issue, as ski resorts are dependent on the snow depth,

slopes, and temperatures, especially for low-altitude ski resorts (Falk, 2010). Specifically, regarding the snow depths, Abegg et al. (2007) evidenced that most of the alpine ski resorts require 100 days each winter with snow depths higher than 30 cm to become cost-effective. Until this point, it has been discussed the importance of snow just in terms of economic revenue, however, snow is also a significant determinant for the ecology of the alpine regions, as it provides natural water storage, reduces erosion and runoff (Barnett et al, 2005), and determine the distribution of plant species (Keller et al, 2005).

Currently, the snow generation system is under high pressure because of the increasing temperatures and the associated rapid melting, accelerated by the continuous cycle of increasing surface temperature and albedo feedback reduction. It has been determined that a 1 ℃ rise in average temperatures, along with winter drought, will reduce the snow cover of areas below 1500 m by 50% (Breiling & Charamza, 1999). Even more, a rise in European temperatures by 1°K would reduce the snow availability in the Austrian Alps for up to 4 weeks in winter and 6 weeks in spring (Hantel et al, 2000). For addressing this problem, different solutions have been proposed and implemented, including the compaction of winter snow cover, injection of liquid water inside the snow cover, and covering of snow with artificial blankets (Olefs & Fischer, 2008). Even though these solutions have proved to work, for example, the artificial blankets solution demonstrated a reduction of 60% in average snow melting rates (Olefs & Fischer, 2008), they are short-term solutions, and their positive impact will be reduced by the increasing temperatures in the following years.

Based on the economic and environmental importance of snow in alpine areas, there is an urgent need for the development and implementation of long-term strategies to effectively address the reduction of Snow-Covered Area (SCA) associated with temperature rise. The proposed strategies must be supported by a strong scientific knowledge base of the status of SCA and temperature trends over the last few years. This will allow a better understanding of the current SCA levels and the validation of the implemented strategies. The objective of this study is to identify spatial-temporal variations of SCA and temperature trends in the Austrian Alps between August 01st of 2018 and July 30th of 2023, through the implementation of Remote Sensing data and techniques, including Landsat 8/Sentinel 2 Satellite Imagery, Land Surface Temperature (LST) products and the Normalized Difference Snow Index (NDSI), within the Google Earth Engine (GEE) cloud-computing platform.

Remote sensing data plays a fundamental role in assessing the SCA and LST (Shrestha et al, 2010). Specifically, Sentinel-2 provides the opportunity to map the snow cover by using the NDSI index from images with 20 m spatial resolution (Gascoin et al, 2020), and Landsat-8 provides LST data at medium spatial resolution (100 m) with the Thermal Infrared Sensor (TIRS) and two adjacent TIR

(Thermal Infrared) bands (Wang et al, 2022). By combining both satellite imagery and data, temperature and SCA trends can be unfolded. Finally, due to the increasing satellite data available and the time-series analysis to be developed in this study, traditional accessing, download, and remote sensing data analysis methods were not suitable. As a result, the data was accessed and analyzed within the GEE platform, which is a cloud computing platform with a multi-petabyte catalog of geospatial datasets (Gorelick et al, 2017), and high computational power that enables large-scale processing of satellite imagery to detect and quantify Earth's surface changes, and map time-series trends (Gandhi, 2021).

2. STUDY AREA

For this study, two selection criteria were applied to different ski areas/resorts, and candidate areas of interest (AOI) in the Austrian Alps. In the first place, considering the spatial resolution for the Sentinel-2 and Landsat-8 bands used (respectively 20 and 100 m), only AOIs big enough to be significantly represented by the associated pixel sizes were considered. It must be clarified that there were no strict size thresholds implemented but rather a preference for the largest AOIs. Secondly, the mean elevation criteria were considered and highly determined the selection of the AOIs. As discussed previously, low-altitude ski resorts are more dependent on temperatures and snow depth. Because of this, it was established that within the selected AOIs, there must be skiing areas located at low altitude (mean altitude less than 1500m) and high altitude (mean altitude higher than 2500m), to evidence the effect of temperature in SCA at different altitudes.

After visually evaluating the performance of the candidate AOIs and considering the study scope and scale, along with the previously mentioned selection criteria, the "Skiwelt Wilder Kaiser - Brixental" (AOI-1) ski resort and the "Komperdell" (AOI-2) skiing area were selected as AOIs. AOI-1 (Figure 1) is one of the largest ski resorts in the world, with over 270 kilometers of ski runs and an area of 37.14 km². Additionally, it is in the Tiroler Unterland Austrian region and is characterized by elevations ranging from 620 to 1869 meters, with a mean altitude of 1202.96 meters (Austria Info, n.d.). On the other hand, AOI-2 (Figure 2) it is in the Tiroler Oberland Austrian region and has an area of 31.36 km² with 214 km of slopes. It consists of different ski resorts, including the "Serfaus-Fiss-Ladis" ski resort, with elevations ranging from 1200 to 2828 meters, and a mean altitude of 2788 meters. (Austrian Info, n.d.)

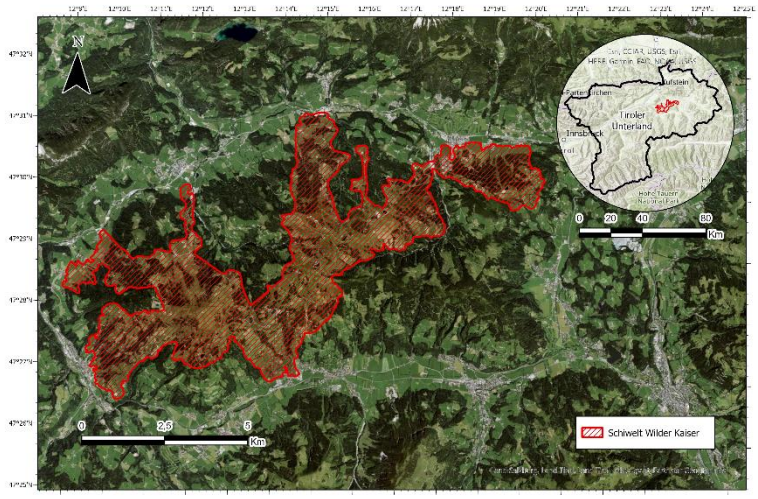

Figure 1. "Skiwelt Wilder Kaiser - Brixental" Ski Resort – AOI-1

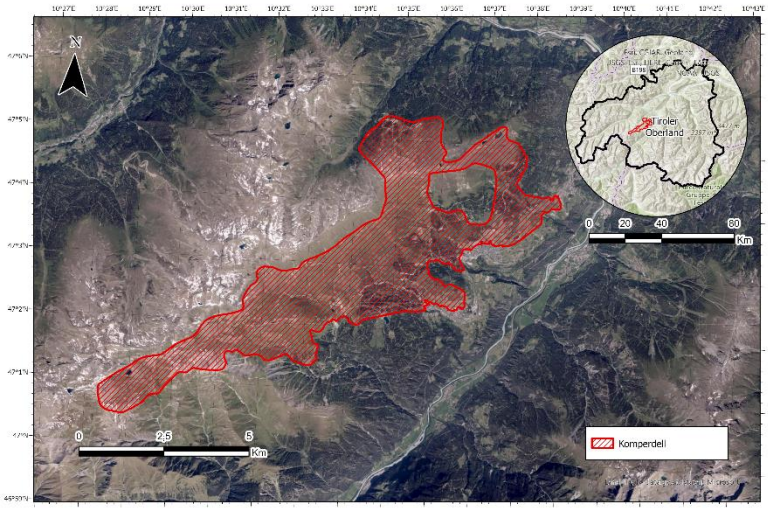

Figure 2."Komperdell" Ski Zone – AOI-2

3. MATERIALS

3.1 SATELITE DATA

3.1.1 SENTINEL 2

The Sentinel-2 mission offers the possibility to capture Earth's land surface at high resolution with a 5-day revisit time and global coverage (Gascoin et al, 2020). Additionally, the high number of spectral bands available (13), including 4 bands at 10 m, 6 bands at 20 m, and 3 bands at 60 m spatial resolution, makes it a unique mission (European Space Agency [ESA], 2014). Satellite Imagery and operational products (e.g., Land Cover Maps) from Sentinel 2 are commonly used in the agricultural

and forestry industry, disaster control, and environmental assessment, including SCA studies using the NDSI index (European Space Agency [ESA], 2014).

In this research, Sentinel-2 (Level 2A) imagery within the study period of interest (2018-08-01 – 2023-07-30), with a "CLOUDY_PIXEL_PERCENTAGE" of less than 10%, from the GEE collection "COPERNICUS/S2_SR_HARMONIZED" was considered. The "CLOUDY_PIXEL_PERCENTAGE" parameter value was selected based on trial-error testing and with the consideration that cloud-masking algorithms were not expected to be applied. Additionally, due to the scope of the study, only spectral bands "B2," "B3," "B4," and "B11" were included (Table 1). As result, 59 images for AOI-1 and 136 images for AOI-2 were retrieved.

BAND NAME	RESOLUTION (m/px)	CENTRAL WAVELENGTH (nm)	USAGE
B2 (Blue)	10	490	Soil and Vegetation discrimination.
B3 (Green)	10	560	Contrast between clear and turbid water.
B4 (Red)	10	665	Identify vegetation types, soils and urban areas.
B11 (SWIR 1)	20	1610	Measure the moisture content of soil and vegetation.

Table 1. Sentinel-2 Bands. Sentinelhub (n.d.)

3.1.2 LANDSAT 8

Landsat 8 was launched on February 11, 2013, and continues the Landsat program's objective of monitoring, understanding, and managing Earth's natural resources (Landsat Missions, 2013). The satellite carries two scientific instruments, the Operational Land Imager (OLI), and the TIRS. OLI provides data for nine spectral bands, all with a spatial resolution of 30 m, except for the Panchromatic band (Band 8 – 15 m). OLI allows capturing Earth's surface in visible, near-infrared, and shortwave-infrared bands. With respect to the TIRS instrument, it measures thermal radiance emitted from the land surface into two infrared thermal bands (Band 10 TIRS and Band 11 TIRS), both with a spatial resolution of 100 m (Landsat Missions, 2013). With those specifications and a revisit time of 16 days, the Landsat 8 mission is crucial for addressing tropical deforestation, urban expansion, water use, climate change, and LST trends.

In this study, Landsat-8 (Level 2) imagery from the “LANDSAT/LC08/C02/T1_L2” GEE collection, between 2018-08-01 and 2023-07-30, and with a “CLOUD_COVER” parameter of less than 30%,

was considered. This parameter value was set up based on the number of images retrieved and the fact that cloud-masking algorithms would be applied, allowing the selection of images with an important presence of clouds and shadows. For each of the images, the spectral bands "SR_B2," "SR_B3," "SR_B4," "ST_B10," and "QA_PIXEL" were included (Table 2). As a result, 76 images for AOI-1 and 83 images for AOI-2 were retrieved.

BAND NAME	RESOLUTION (m/px)	CENTRAL WAVELENGTH (nm)	USAGE
SR_B2 (Blue - Surface Reflectance)	30	482	Soil and Vegetation discrimination.
SR_B3 (Green - Surface Reflectance)	30	560	Contrast between clear and turbid water.
SR_B4 (Red - Surface Reflectance)	30	655	Identify vegetation types, soils and urban areas.
ST_B10 (Surface Temperature)	100	1090	Measure Surface Temperature in Kelvin.
QA_PIXEL (Cloud and Shadow bitmaks)	-	-	Apply cloud, snow and water bitmask.

Table 2. Landsat 8 Bands. Earth Engine Data Catalogue (n.d.)

3.2 GOOGLE EARTH ENGINE (GEE)

As mentioned previously, GEE is a cloud computing platform that provides access to high amounts of satellite imagery and processing large-scale capabilities that allow the analyses of thousand images simultaneously in the cloud, without requiring to download the data locally. The first GEE version was launched in 2010, with the objective of addressing big data challenges, including the acquisition, storage, searching, analysis, and visualization of huge amounts of data (Liu, 2015). In addition to the computational power and satellite imagery collections, GEE provides JavaScript and Python API functionalities, along with operations like Clip, Band Math, Composite bands, Map, and Reduce.

Because of those characteristics, GEE is currently the most well-performing cloud computing platform for working with satellite imagery on environmental and disaster monitoring, climate change studies, weather analysis, and most importantly, time-series analysis. As a result, for the study case proposed in this paper, the methodology (data preparation, analysis, and results visualization) was developed 100% within this platform.

4. METHODOLOGY

The proposed methodology (Figure 3) was developed within the GEE platform with Sentinel-2 and Landsat 8 image collections. The full code can be accessed through the following link: GEE code.

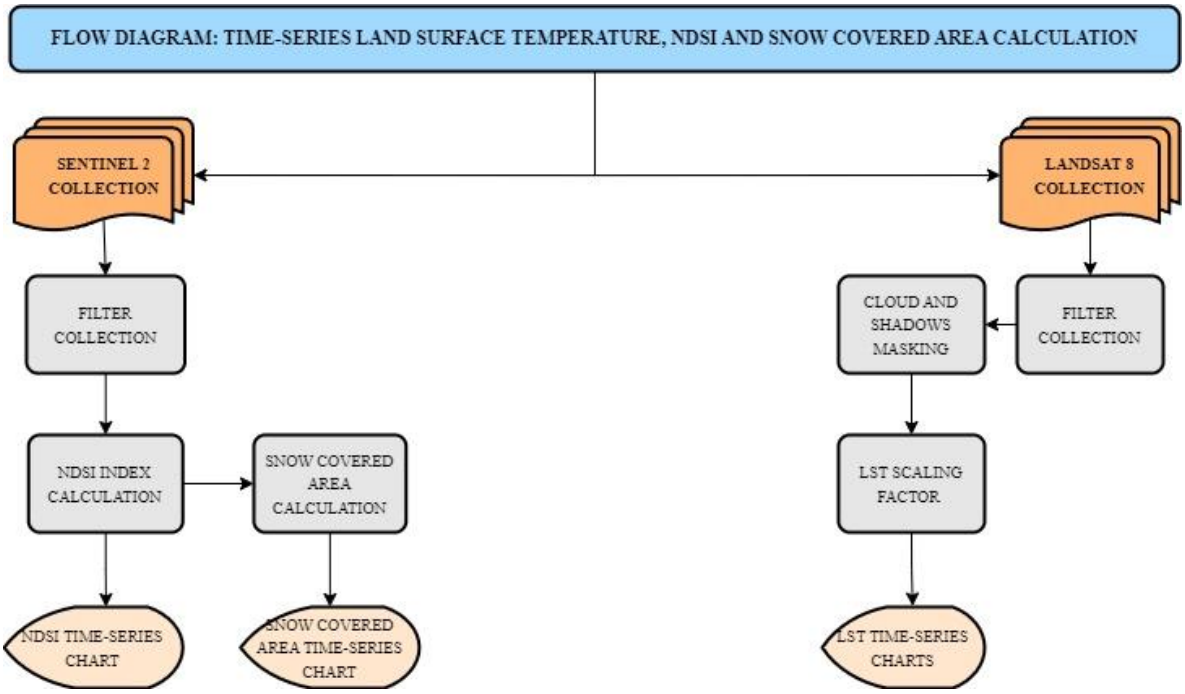

Figure 3. Methodology in GEE.

4.1 SENTINEL 2

4.1.1 FILTER COLLECTION

The Sentinel-2 collection was filtered based on the AOIs bounds, dates, and the "CLOUDY_PIXEL_PERCENTAGE," as described in Section 3.1.1 For this process, an image collection ("sentinel_collection") was defined using the "ee.ImageCollection()" function. (Code Section 1)

```
var sentinel_collection = ee.ImageCollection("COPERNICUS/S2_SR_HARMONIZED")
.filterBounds(AOI)
.filterDate("2018-08-01", "2023-07-30")
.filterMetadata("CLOUDY_PIXEL_PERCENTAGE", "less_than",10)
.select(["B2", "B3", "B4", "B11"])
```

Code Section 1. Sentinel 2 Collection – Filter.

4.1.2 NDSI INDEX CALCULATION

The NDSI is a numerical indicator that shows snow cover over land areas using the green and short-wave infrared (SWIR) spectral bands (Hall et al., 1995). One of the main characteristics of the NDSI index (see Figure 4) is the fact that due to the high reflectance of snow in the visible bands and low

reflectance in the near infrared (Rabatel et al., 2012) it can distinguish snow and ice from other features, including clouds and shadows. This was the reason behind the decision of not applying cloud-masking algorithms to the Sentinel-2 Collection.

$$\boldsymbol{NDSI(Sentinel\ 2)} = \frac{B3 - B11}{B3 + B11}$$

Figure 4. NDSI Index Formula (Sentinel 2).

For calculating the NDSI index in GEE for each image of the collection, the function "ndsi_index" was created. It uses the "normalizedDifference()" function with bands "B3" and "B11" as parameters. As a result, it adds the "NDSI" band to each image of the collection and clips the image to the corresponding AOI extent. (Code Section 2)

```
var ndsi_index = function(image){
   var ndsi = image.normalizedDifference(["B3","B11"])
   image = image.addBands(ndsi.rename("NDSI"))
   return image.clip(AOI)
 }
```

Code Section 2. Sentinel 2 Collection – NDSI Index and clipping Function.

4.1.3 SNOW COVERED AREA CALCULATION

According to Wang et al. (2018), the NDSI suggested threshold is 0.35; however, with trial-and-error testing, the threshold for SCA was defined as 0.40. Considering the above and the NDSI index calculation performed in section 4.1.2, the "calculateSnowArea()" function was defined. In this function, pixels with NDSI index values greater than or equal to 0.4 are stored into a new variable called "snowMask." Then, their pixel area is divided by 1,000,000 (to have units in square kilometers), and the results are stored in the "snowArea" variable. In this variable, pixels that are considered as SCA will have a value of 0.000667517 square kilometers (corresponding to the pixel size in km2), and the others will have a value of 0, representing pixels without snow. As a result, for each image of the collection, the band "Snow_Area" is added with the values from the "snowArea" variable. (Code Section 3)

```
var calculateSnowArea = function(image){
   var snowMask = image.select("NDSI").gte(0.4)
   var snowArea = snowMask.multiply(ee.Image.pixelArea()).divide(1000000)
   return image.addBands(snowArea.rename("Snow_Area"))
 }
```

Code Section 3. Sentinel 2 Collection – Snow Area Calculation Function.

4.1.4 TIME-SERIES CHARTS

Finally, for both the NDSI index and SCA values, time-series charts were created. The mean NDSI value per image in the image collection was calculated (independently for each AOI). Then, the time-series chart was generated using the "iu.Chart.image.seriesByRegion()" function, with parameters like the collection (sentinel_collection), the AOI, the reducer to be applied (mean), and the scale (10). (Code Section 4)

```
var graphicNDSI = ui.Chart.image.seriesByRegion(sentinel_collection, AOI, ee.Reducer.mean(),
"NDSI", 10, null, "NAME")
.setChartType("LineChart")
.setOptions(NDSI_options);
print(graphicNDSI)
```

Code Section 4. Sentinel 2 Collection – NDSI Index Time-Series Chart Function.

Regarding the time-series chart for SCA, the "ui.Chart.image.seriesByRegion()" function was used one more time, with similar parameters as in Code Section 4. However, instead of using a "mean" reducer, the "sum" reducer was used with the purpose of summing the "Snow_Area" band, which represents the area of each pixel. As a result, the total SCA per image was calculated and displayed as a time-series chart. (Code Section 5)

```
var graphicSNOW = ui.Chart.image.seriesByRegion(sentinel_collection, AOI, ee.Reducer.sum(),
"Snow_Area", 10, null, "NAME")
.setChartType("LineChart")
.setOptions(Snow_Area_options);
print(graphicSNOW)
```

Code Section 5. Sentinel 2 Collection – SCA Time-Series Chart Function.

4.2 LANDSAT-8

4.2.1 FILTER COLLECTION

As described in Section 3.1.2, the Landsat 8 Collection was filtered considering the "CLOUD_COVER" data and AOI boundaries. The result was the "*landsat_collection*" image collection. (Code Section 6)

```
var landsat_collection = ee.ImageCollection('LANDSAT/LC08/C02/T1_TOA')
  .filterMetadata ('CLOUD_COVER', 'less_than', 30)
  .filterDate("2018-08-01", "2023-07-30")
  .filterBounds(AOI)
```

Code Section 6. Landsat 8 Collection – Filter.

4.2.2 CLOUD AND SHADOWS MASKING

Considering that LST values could be affected by the presence of clouds or shadows, the "*masking()*" function was implemented for the Landsat 8 Collection (Code Section 7).

```
var masking = function(image){
   var cloudBitMask = (1<<3);
   var cloudShadowBitMask = (1<<4);
   var qa = image.select("QA_PIXEL");
   var mask = qa.bitwiseAnd(cloudShadowBitMask).eq(0)
   .and(qa.bitwiseAnd(cloudBitMask).eq(0))
   return image.updateMask(mask);
   }
```

Code Section 7. Landsat 8 Collection – Clouds and Shadows Masking Function.

The function receives as input each of the images of an Image Collection and removes unwanted cloud and cloud shadow artifacts using bitmasks and bitwise operations. It uses the "*QA_PIXEL*" band from the image to access the cloud and cloud shadow flags (Bit 3 and Bit 4, respectively) and creates boolean masks for cloud-free and shadow-free pixels. As a result, the algorithm produces images without the mentioned artifacts that can affect the LST measures (Figure 5).

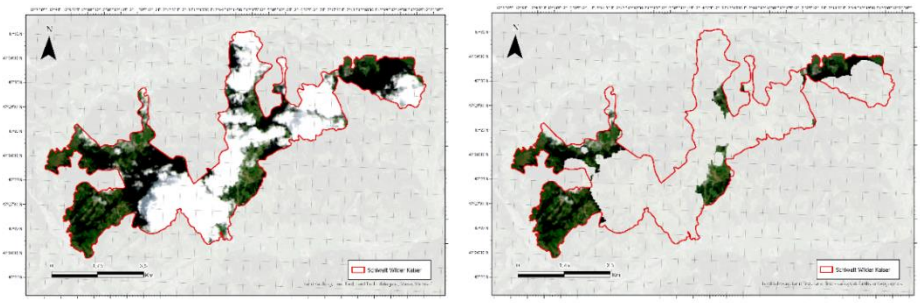

Figure 5. **Left:** Landsat 8 Image (AOI-1) without the masking() algorithm implemented. **Right:** Landsat 8 Image (AOI-1) with the masking() algorithm implemented

4.2.3 LST SCALING FACTOR

Landsat 8 measures the LST in the band "ST_B10" using Kelvin units. However, certain scaling factors must be applied to adjust the measurements for this study. To achieve this, the "*ScaleFactorLST()*" function was developed. This function selects the "*ST_B10*" band for each image in the image collection and applies a series of operations: it multiplies the values by 0.00341802 (the scale factor), adds 149 (the offset), and fianlly adds -273.15 to convert the values from Kelvin to Celsius degrees. After this function is applied, each image in the collection will include a new band representing the LST in Celsius degrees. (Code Section 8)

```
var ScaleFactorLST = function (image) {
   var thermalBands = image.select('ST_B.*').multiply(0.00341802).add(149.0).add(-273.15);
  return image.addBands(thermalBands, null, true).clip(AOI);
}
```

Code Section 8. Landsat 8 Collection – LST Scaling Factor Function.

4.2.4 TIME-SERIES CHART

As for the Sentinel-2 Collection, the "*ui.Chart.image.seriesByRegion()*" function was implemented, using the "*mean()*" reducer and a spatial resolution of 100m, which is associated with the spatial resolution of the thermal band. This function reduces the LST values of each of the images by taking the mean and generates a "*LineChart*" time-series graphic. (Code Section 9)

```
var graphicLST_L2 = ui.Chart.image.seriesByRegion(landsat_collection, AOI, ee.Reducer.mean(),
"ST_B10", 100, null, "NAME")
.setChartType('LineChart')
.setOptions(LST_options_L2);
print(graphicLST_L2)
```

Code Section 9. Landsat 8 Collection – LST Time-Series Chart Function.

5. RESULTS

5.1 SKIWELT WILDER KAISER – BRIXENTAL

5.1.1 NDSI INDEX AND TIME-SERIES CHART

After calculating the NDSI Index values for each image, adding them as a new band in the feature collection, and visually evidence the correct identification of SCA (Figure 6), the NDSI Index time series chart was created (Figure 7).

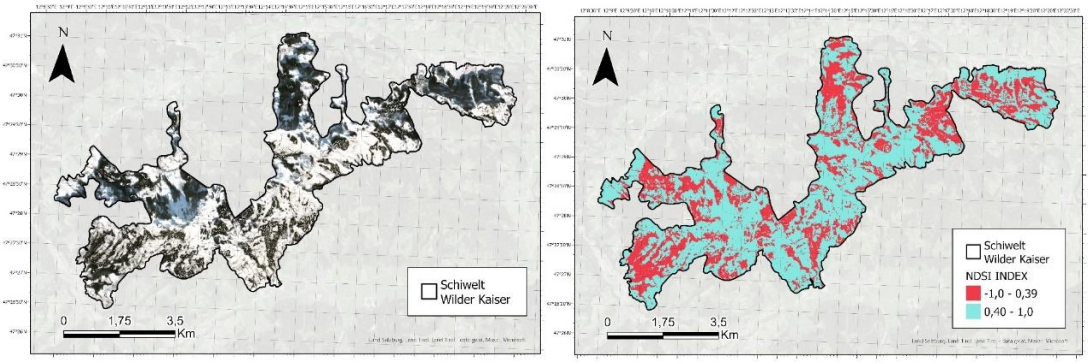

Figure 6. Left: AOI-1 RGB Composite (Sentinel 2). **Right:** AOI-1 NDSI Index. (2020-02-08).

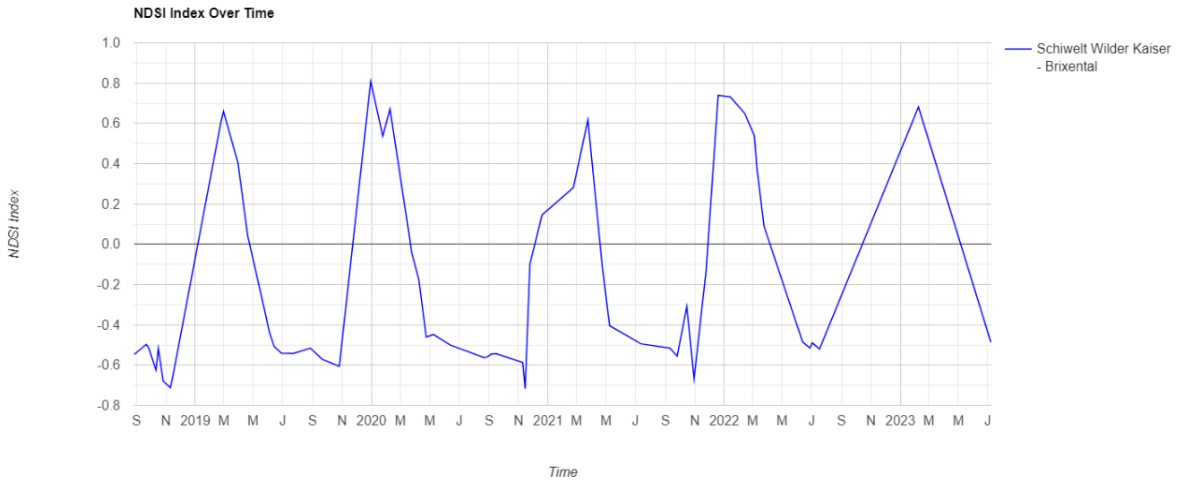

Figure 7. AOI-1 NDSI Index Time-Series Chart.

Regarding the NDSI Index Time-Series chart, the most significant aspects are the maximum and minimum mean NDSI Index values over the study period. In 2018, the minimum NDSI Index value was -0.712, observed on November 10. Moving to 2019, two maximum peaks are evident. The first one corresponds to a value of 0.659 (recorded on February 28), and the second one reaches 0.808 (achieved on December 30). The minimum value in 2019 was -0.605, observed on October 26. In 2020, the maximum NDSI Index mean value reached 0.671, recorded on February 8, while the minimum was -0.717 (measured on November 14). The maximum value for 2021 occurred on March 24, measuring 0.617, whereas the minimum was registered on October 30, with a value of -0.667. For 2022, the maximum value was 0.732 (measured on January 13), and the minimum was -0.52 on July 17. Finally, for 2023, the maximum registered was 0.681, observed on February 7, while the minimum (up to date) was -0.486, registered on July 7.

5.1.2 SCA TIME-SERIES CHART

As explained in previous sections, the SCA was calculated based on the NDSI index and the defined threshold (0.40), and the SCA Time-Series Chart was created (Figure 8). The most significant feature in this case was the maximum SCA observed during the study period. In 2019, the maximum SCA value reached 28.588 km2 (on February 28). Moving to 2020, the highest value registered was 34.840 km2 (on December 30). In 2021, the maximum SCA was observed on March 24, corresponding to 28.855 km2. Concerning 2022, the maximum value reached 31.497 km2 (on January 17). Finally, in 2023, the maximum SCA value measured was 32.016 km2, recorded on February 7.

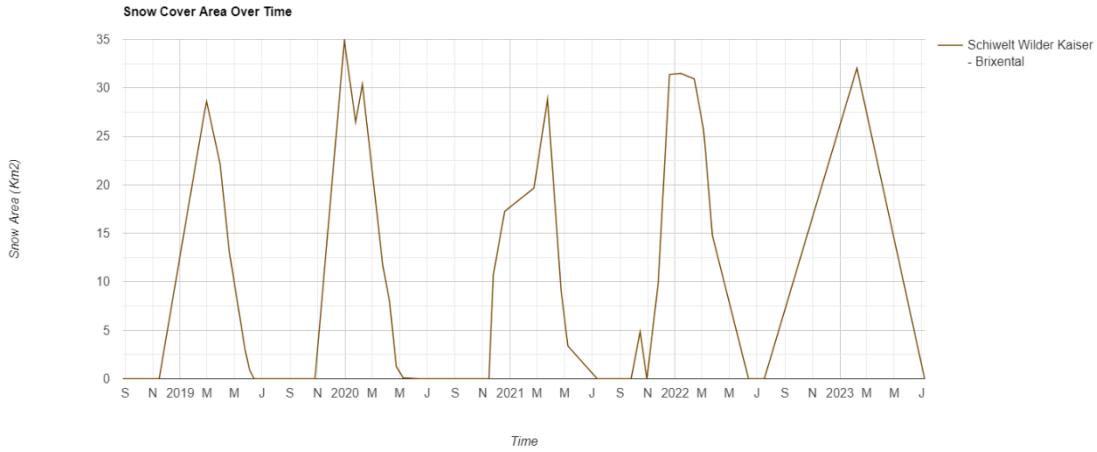

Figure 8. AOI-1 SCA Index Time-Series Chart.

5.1.3 LST AND TIME-SERIES CHART

The LST values resulting from the Landsat 8 Thermal band were visually checked to confirm the correct implementation of the proposed workflow, including cloud and shadow masking and coherent LST values. This verification process was conducted for several images, including the Landsat 8 image from May 9, 2020 (Figure 9).

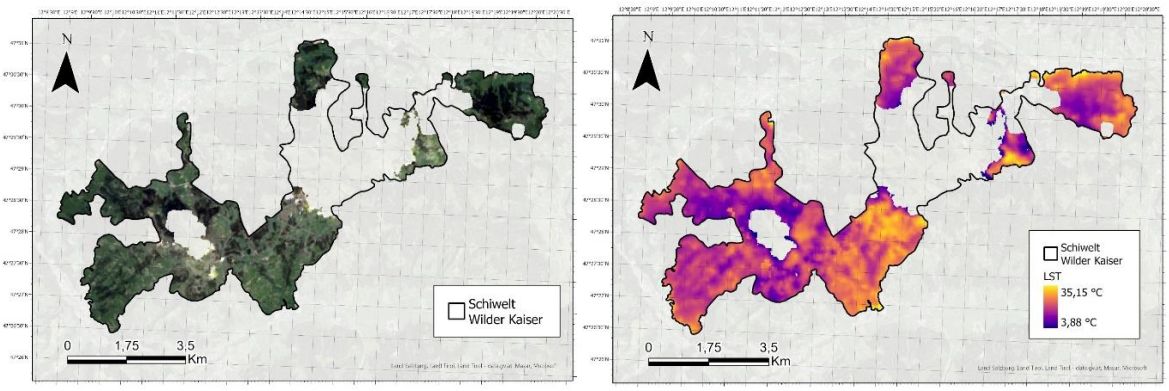

Figure 9. Left: AOI-1 RGB Composite (Landsat 8). **Right:** AOI-1 LST.

Once it was confirmed that the LST values were accurate, the LST Time-Series Chart (Figure 10) was generated. The most significant features of the LST over the study period were the maximum and minimum peaks. In 2018, the maximum mean temperature recorded was 30.62 °C on August 1, while the minimum temperature was observed on December 14, corresponding to -11.39 °C. Moving to 2019, the maximum LST was 27.27 °C on June 24, and the minimum was -3.92 °C on December 26. In 2020, the highest LST peak was seen on July 28, reaching 28.99 °C, and the minimum LST was -10.207, recorded on February 14. For 2021, the maximum value reached 29.74 °C, and the minimum was -8.30 °C. In 2022, the highest LST occurred on August 3, with a value of 27.18°C, while there were two minimums: the first on April 13, with -10.82 °C, and the second on December

18, corresponding to an LST of -8.37 °C. Finally, the maximum LST recorded in 2023 (up to date) is 25.61 °C, observed on June 3.

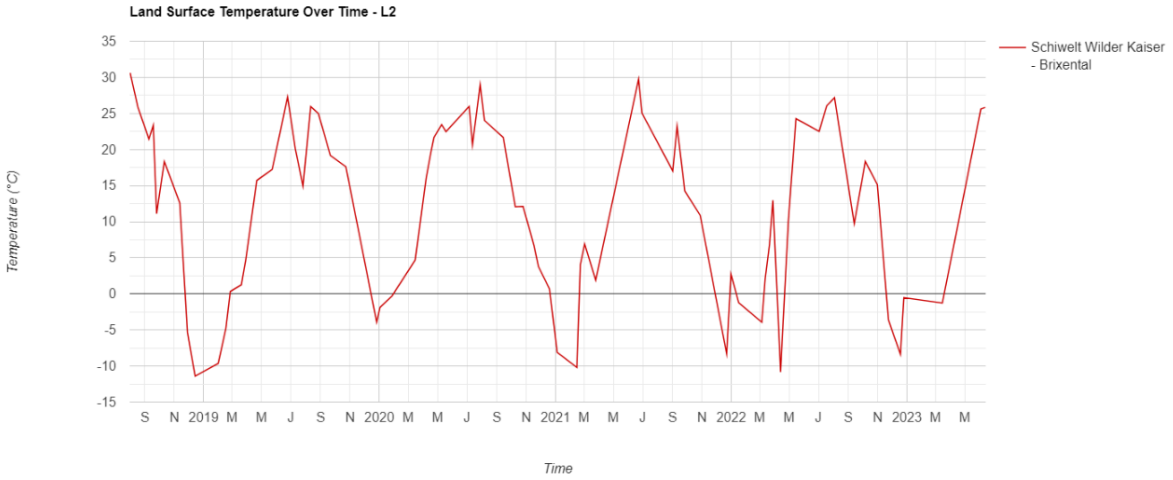

Figure 10. AOI-1 LST Time-Series Chart.

5.2 KOMPERDELL

As for AOI-1, various NDVI Indexes images were visually checked to confirm the correct identification and delineation of SCA, without the influence of clouds and shadows (Figure 11). Once the 0.4 threshold was confirmed to fit the study purpose the best, the NDVI Index Time-Series chart was created (Figure 12).

5.2.1 NDSI INDEX AND TIME-SERIES CHART

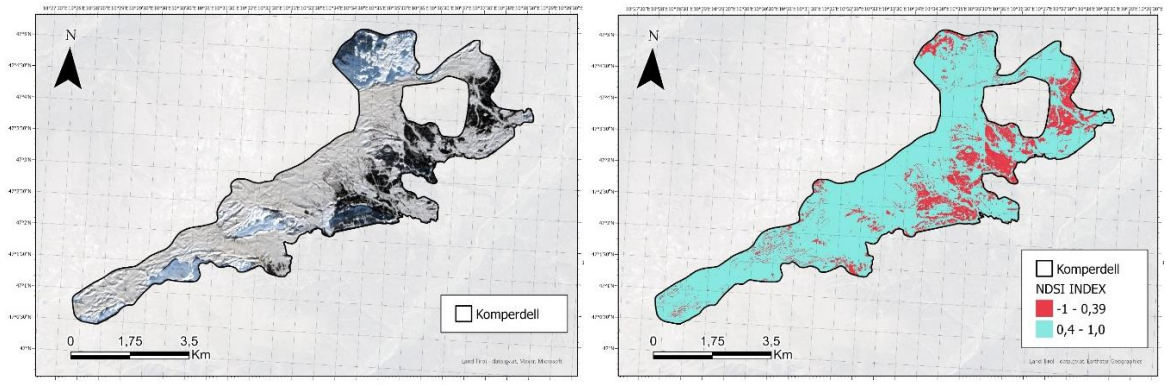

Figure 11. Left: AOI-2 RGB Composite (Sentinel 2). **Right:** AOI-2 NDSI Index. (2023-02-07)

As mentioned in section 5.1.1, the key aspect to identify from the Time-Series chart was the maximum and minimum NDVI index values over the study period.

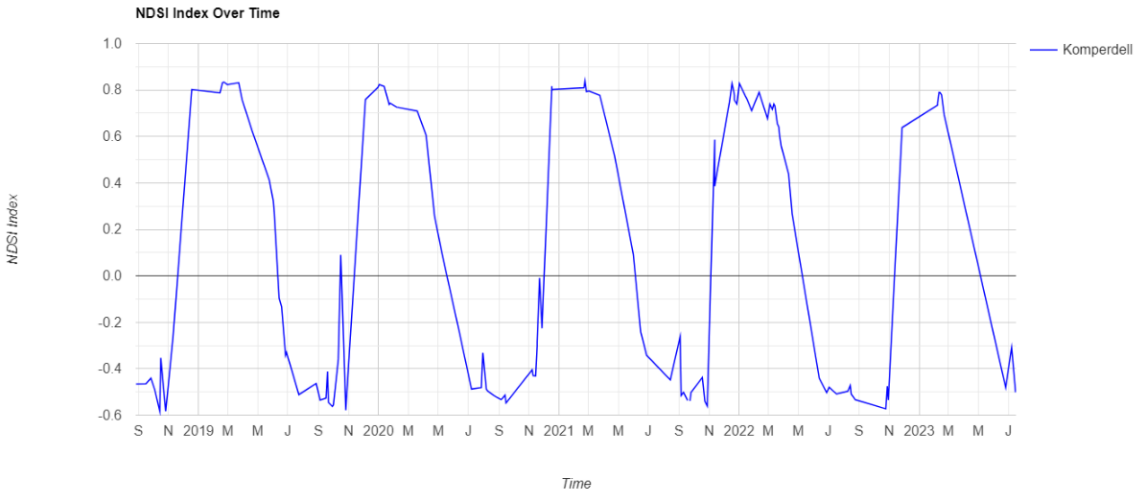

Figure 12. AOI-2 NDSI Index Time-Series Chart.

In 2018, the minimum NDSI Index value of -0.583 was recorded on October 26, while the maximum value of 0.802 was registered on December 18. Moving on to 2019, the maximum NDSI Index value was 0.831, observed on March 23, and the minimum value was -0.578, measured on October 26. For the year 2020, the maximum value of 0.823 was noted on January 2, and the minimum NDSI Index value of -0.547 was registered on September 15. In 2021, the maximum value of 0.839 was observed on February 22, and the minimum value of -0.54 occurred on October 28. As for 2022, the maximum NDSI Index value of 0.828 was recorded on January 1, and the minimum value of -0.573 occurred on October 25. Lastly, as of the latest data available in 2023, the maximum NDSI Index value of 0.789 was registered on February 10.

5.2.2 SCA TIME-SERIES CHART

According to the SCA Time-Series chart (Figure 13), the maximum SCA values for each year are as follows: in 2018, it was 30.319 km2, registered on December 18. In 2019, there were two maximum peaks, one on March 23, with a value of 29.015 km2, and the second one in December, reaching 30.146 km2. Moving to 2020, the highest SCA was evidenced at 31.281 km2, registered on February 6. For 2021, the maximum SCA value was recorded on February 20, with a coverage of 29.856 km2. As for the rest of 2021, on December 12, the maximum SCA reached 29.649 km2. In 2022, the peak SCA value occurred on February 10, measuring 29.284 km2. Additionally, up to the current date in 2023, the maximum SCA registered was 30.296 km2, evidenced on February 7. It is worth mentioning that there is a notable low SCA peak recorded on February 25, 2021, with a value of 3.615 km2.

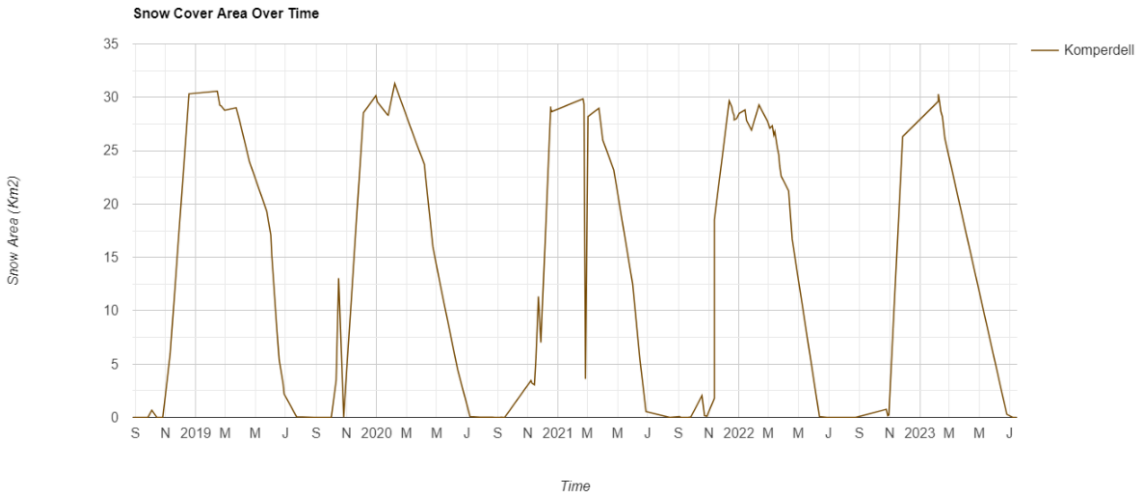

Figure 13. AOI-2 SCA Index Time-Series Chart.

5.2.3 LST AND TIME-SERIES CHART

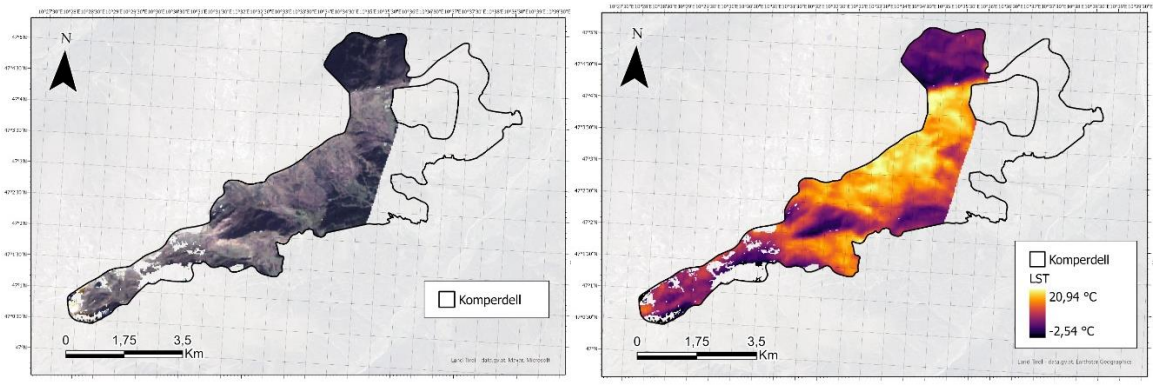

Figure 14. Left: AOI-2 RGB Composite (Landsat 8). **Right:** AOI-2 LST.

For AOI-2, the visual validation of the LST was carried out, following the same process as for AOI-1. This validation process was implemented for various images, including the Landsat 8 image taken on October 29, 2022 (Figure 14). Particularly in this image, it is evident that areas not directly exposed to the sun have lower temperatures. Additionally, the image appears to be clipped on the East side. Once the visual validation was completed, the LST Time-Series Chart was created (Figure 15).

On the LST Time-Series Chart, it can be observed that for 2018, the highest LST was registered on September 9, reaching 23.62 °C. On the other hand, the lowest LST of -14.5 °C was recorded on December 14. Moving to 2019, the maximum LST occurred on June 24, with a value of 29.42 °C, while the minimum LST of -6.70 °C was recorded on December 6. Moving to 2020, the highest LST peak was recorded on July 28, reaching a temperature of 28.53 °C. Conversely, the lowest LST for that year was -15.40 °C, recorded on December 26. As for 2021, there were two important minimum peaks, recorded on February 12 and December 22, with LST values of -12.56 °C and -8.82 °C,

respectively. Regarding the maximum LST, it was registered on July 6, reaching 27.92 °C. In 2022, the highest LST occurred on July 18, with a temperature of 29.33 °C, while the lowest LST was -9.56 °C, registered on November 23. Finally, for 2023, the highest LST value registered up to date is 28.70 °C (measured on June 26), and the lowest is -8.91 °C, corresponding to January 1.

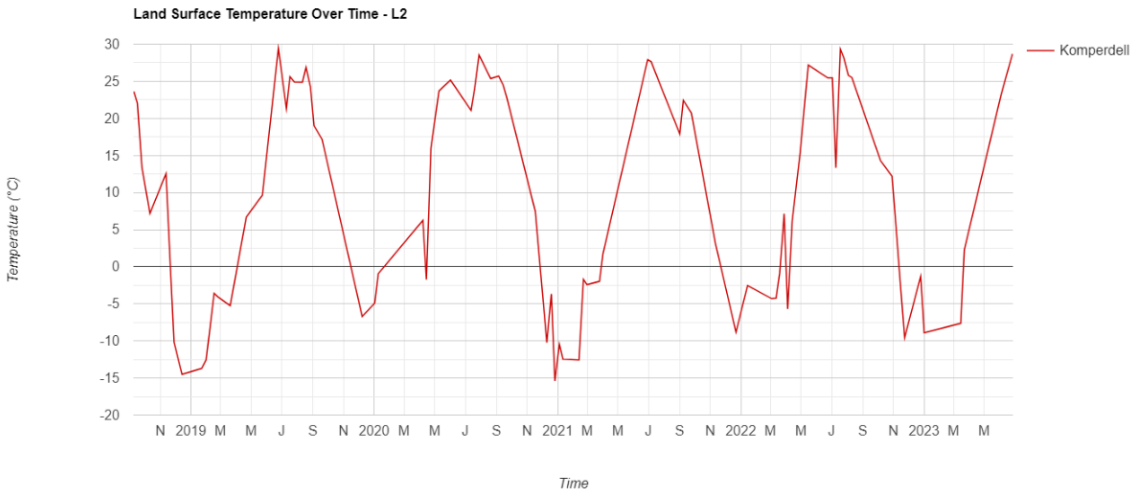

Figure 15. AOI-2 LST Time-Series Chart.

6. DISCUSSION

Firstly, the NDVI Index (with a threshold of 0.40) applied to the AOI-1 and AOI-2 proved to work effectively. Using this spectral index, most of the SCA was identified correctly, including zones with the presence of cloud shadows and light clouds. However, in some of the manually verified images, small portions of dense clouds were misclassified as snow. As a result, there is a possibility of overestimating the SCA. Considering the above, it is recommended to apply a cloud and shadow mask algorithm to the Sentinel 2 collection, which was used for calculating the NDSI Index and deriving the SCA.

Regarding the NDSI Index time-series chart, specifically for AOI-1 and using the highest NDSI index value in 2019 as a reference, it can be observed that in 2020, 2022, and 2023, the maximum NDSI index values were greater than those in 2019. However, the maximum NDSI index value for 2021 was smaller in comparison to 2019. With these results, it would be expected that in 2020, 2022, and 2023, there would be higher SCA values compared to 2019, and less SCA in 2021. This can be partially confirmed with the SCA time-series chart, as the days with the highest SCA values for 2020, 2022, and 2023 were indeed higher. However, the highest SCA day in 2021 was also higher than in 2019, which, according to the NDSI, shouldn't be the case. As a result, between 2018 and 2023, the day with the most SCA was in 2020, while the lowest was in 2019. Moreover, the SCA has increased each year from 2021. This trend could be explained by two factors. First, the implementation of short-

term solutions related to the low SCA evidenced in previous years, which included the use of thermal blankets or artificial snow. And secondly, there is a possible decrease in LST in recent years.

Based on the NDSI Index and derived SCA values, it can be determined that the suggested workflow fits the requirement of calculating the snow extent in square kilometers. Nevertheless, as the generated output is the SCA for each day an image was captured, the interpretation of the SCA tendencies could be affected by daily anomalies. Because of this, for a better understanding of SCA changes between 2018 and 2023, it would be required to reduce the number of images per year or season (summer or winter).

By analyzing the LST temperature time-series chart, it was determined that since 2021, the highest temperature registered each of the following years has been lower, and possibly the mean temperature too. The reduction in the LST in the last three years supports (as mentioned before) the fact that SCA has increased since 2021. However, the LST analysis would benefit from the reduction of the study to mean values by year or by seasons. For this study, due to time and data constraints, an extensive LST validation was not performed. However, a quick comparison with Austrian temperature stations was carried out, and as a result, an overestimation of 2 °C of the LST estimated through Landsat 8 was observed. To address this situation, additional LST estimation methods (e.g., Convert Landsat 8 level-1 Brightness Temperature) must be implemented to validate Landsat 8 values.

Moving to AOI-2, there is a noticeable change in the NDSI Index and associated SCA tendencies observed through the Time-Series charts. In contrast to the behavior of AOI-1 with strong maximum and minimum peaks, in the AOI-2, it can be observed that both NDSI index and SCA values are more stable. This means that the NDSI index values and SCA are considerably higher for this AOI for longer periods of time. This is explained by the fact that the AOI-2 skiing area is located at a higher altitude in comparison to AOI-1. Therefore, the temperatures are expected to be lower during most of the year, which facilitates the generation of snow and reduces melting rates. As a result, the maximum SCA value registered for each year between 2018 and 2023 is on average 30 km2. Additionally, the months between December and March are the ones where the SCA is the highest, while between June and October, it is the lowest, corresponding to winter and summer seasons, respectively.

With respect to the LST values observed in the related Time-Series chart, it was not expected to observe a similar trend with respect to AOI-1 LST. However, even though the maximum temperatures in both study areas are closer, the minimum temperatures observed in winter for the AOI-2 are 2-4 degrees Celsius less than AOI-1. Consequently, it can be evidenced that during the winter in the AOI-

2 area, due to the low temperatures, more snow accumulates, and it takes more time to melt during summer, resulting in higher SCA, greater stability, and distinct seasonality.

In overview, for both areas of study, AOI-1 and AOI-2 LST and SCA trends were identified. Specifically, in AOI-1, it was observed that in the last few years, the maximum temperature registered has decreased, and consequently, the maximum SCA extent has increased. However, that behavior could be related to the short-term solutions implemented to reduce snow melting in the area. Moreover, it was observed that there is less SCA and stability (shown by the narrow maximum peaks) in comparison to AOI-2. Finally, even though AOI-2 shows a similar LST trend as AOI-1, the SCA stays constant over the study period (fluctuating based on the seasonality). This is related to the mean high-altitude location, which facilitates snow generation and stability.

7. CONLUSIONS

In conclusion, remote sensing techniques (like NDSI Index calculation), satellite imagery, and the GEE cloud-computing platform proved to be outstanding tools for addressing SCA calculations, LST estimations, and Time-Series charts. This study greatly benefited from the GEE cloud-computing platform as more than 200 satellite images were included in the analysis without requiring downloading any of them. Additionally, making use of the Google servers, the time series charts, and raster products were generated faster than using traditional methods.

Regarding the SCA calculation, the NDSI Index algorithm and threshold established to count a pixel as snow cover worked as expected and produced coherent km2 values. However, due to the misclassification of some clouds as snow pixels and the lack of validation data, some changes are recommended for further studies, including the application of cloud masking algorithms to the Sentinel 2 Image Collection and the validation of the SCA values obtained with Austrian official data sources. Additionally, even though the SCA and NDSI Index trends were identified, focusing the discussion on daily behaviors can lead to wrong conclusions, as the data could have been altered by daily anomalies. Because of this, it is recommended for further research to reduce the data by means of determined periods of time (years or seasons). In this way, the influence of daily anomalies is reduced, and the results are more representative.

Regarding the LST data retrieved and converted from the Landsat 8 thermal band, it accurately represents temperature changes in areas with snow, shadows, and vegetation, which gives an idea of the accuracy of the processing performed by the data provider. However, in comparison to Austrian official data sources, there was evidence of an overestimation of approximately 2°C of the LST measured by Landsat 8. As a result, even though the data and LST trends discussed in this study are

valid, it is recommended to explore other LST alternatives like the usage of MODIS imagery or Landsat 8 – Level 1 imagery to convert brightness into Surface Temperature based on the corresponding surface emissivities derived from the NDVI Index. Having mentioned this recommendation, the LST discussion carried out showed in the first place how high altitudes prevent the snow from melting at faster rates, leading to high SCA values. In this aspect, during the last five years, both AOIs demonstrated to have constant SCA extents, but it is a fact that low-altitude skiing areas will be more and more exposed to snow reduction because of melting related to an increase in global temperatures.

Finally, this study serves as the basis for SCA and LST analysis within cloud computing platforms like GEE. It is expected that further research explores their possibilities and, even more, considers and applies the recommendations presented in this article.

7. REFERENCES

Abegg, B., Agrawala, S., Crick, F., & de Montfalcon, A. (2007). Climate change impacts and adaptation in winter tourism. Climate change in the European Alps: Adapting winter tourism and natural hazards management, 25-58.

Austria Info. (n.d). The 10 largest ski areas in Austria. Retrieved from https://www.austria.info/en/things-to-do/skiing-and-winter/skiing/largest-ski-resorts

Barnett, T. P., Adam, J. C., & Lettenmaier, D. P. (2005). Potential impacts of a warming climate on water availability in snow-dominated regions. Nature, 438(7066), 303–309. https://doi.org/10.1038/nature04141

Breiling, M., & Charamza, P. (1999). The impact of global warming on winter tourism and skiing: a regionalised model for Austrian snow conditions. Regional Environmental Change, 1, 4-14.

Earth Engine Data Catalogue (n.d.). USGS Landsat 8 Level 2, Collection2, Tier 1. Retrieved from https://developers.google.com/earth-engine/datasets/catalog/LANDSAT_LC08_C02_T1_L2

European Space Agency [ESA]. (2014). Sentinel-2 overview. Retrieved from https://www.esa.int/Applications/Observing_the_Earth/Copernicus/Sentinel-2_overview

Falk, M. (2010). A dynamic panel data analysis of snow depth and winter tourism. Tourism Management, 31(6), 912-924.

Gandhi, U. (2021). End-to-End Google Earth Engine Course. Spatial Thoughts. Retrieved from https://courses.spatialthoughts.com/end-to-end-gee.html

Gascoin, S., Barrou Dumont, Z., Deschamps-Berger, C., Marti, F., Salgues, G., López-Moreno, J. I., ... & Hagolle, O. (2020). Estimating fractional snow cover in open terrain from sentinel-2 using the normalized difference snow index. Remote Sensing, 12(18), 2904.

Gorelick, N., Hancher, M., Dixon, M., Ilyushchenko, S., Thau, D., & Moore, R. (2017). Google Earth Engine: Planetary-scale geospatial analysis for everyone. Remote sensing of Environment, 202, 18-27.

Hall, D. K., Riggs, G. A., & Salomonson, V. V. (1995). Development of methods for mapping global snow cover using moderate resolution imaging spectroradiometer data. Remote sensing of Environment, 54(2), 127-140.

Hantel, M., Ehrendorfer, M., & Haslinger, A. (2000). Climate sensitivity of snow cover duration in Austria. International Journal of Climatology: A Journal of the Royal Meteorological Society, 20(6), 615-640.

Hruby, D. (2020). In the Alps, ski resorts are desperately battling climate change-and local resistance. Retrieved from https://www.nationalgeographic.com/environment/article/alps-ski-resorts-desperately-battling-climate-change-local-resistance?rnd=1684484358068&loggedin=true

Keller, F., Goyette, S., & Beniston, M. (2005). Sensitivity analysis of snow cover to climate change scenarios and their impact on plant habitats in alpine terrain. Climatic Change, 72(3), 299-319.

Landsat Missions (2013). Landsat 8. Retrieved from https://www.usgs.gov/landsat-missions/landsat-8

Liu, P. (2015). A survey of remote-sensing big data. frontiers in Environmental Science, 3, 45.

Moreno-Gené, J., Sánchez-Pulido, L., Cristobal-Fransi, E., & Daries, N. (2018). The economic sustainability of snow tourism: The case of ski resorts in Austria, France, and Italy. Sustainability, 10(9), 3012.

Olefs, M., & Fischer, A. (2008). Comparative study of technical measures to reduce snow and ice ablation in Alpine glacier ski resorts. Cold regions science and technology, 52(3), 371-384.

Rabatel, A., Bermejo, A., Loarte, E., Soruco, A., Gomez, J., Leonardini, G., ... & Sicart, J. E. (2012). Can the snowline be used as an indicator of the equilibrium line and mass balance for glaciers in the outer tropics?. Journal of Glaciology, 58(212), 1027-1036.

Sentinelhub (n.d.). Sentinel-2 Bands. Retrieved from https://custom-scripts.sentinel-hub.com/custom-scripts/sentinel-2/bands/

Shrestha, R.K., Ahlers, R., Bakker, M.B., and Gupta, J. (2010). Institutional dysfunction and challenges in flood control along the transboundary Koshi River: A case study of the Kosi Flood 2008, Econom. Polit. Weekly, 2010, vol. 45, pp. 45–53.

Tamiminia, H., Salehi, B., Mahdianpari, M., Quackenbush, L., Adeli, S., & Brisco, B. (2020). Google Earth Engine for geo-big data applications: A meta-analysis and systematic review. ISPRS Journal of Photogrammetry and Remote Sensing, 164, 152-170

Wang, M., Li, M., Zhang, Z., Hu, T., He, G., Zhang, Z., ... & Liu, X. (2022). Land Surface Temperature Retrieval From Landsat 9 TIRS-2 Data Using Radiance-Based Split-Window Algorithm. IEEE Journal of Selected Topics in Applied Earth Observations and Remote Sensing, 16, 1100-1112.

Wang, X., Chen, H., & Chen, Y. (2018). Topography-Related Glacier Area Changes in Central Tianshan from 1989 to 2015 Derived from Landsat Images and ASTER GDEM Data. Water, 10(5), 555

Wertschöpfung durch österreichische Seilbahnen. (2021). Retrieved from https://www.wko.at/branchen/transport-verkehr/seilbahnen/Wertschoepfung-durch-oesterreichische-Seilbahnen.html